PHYSICAL REVIEW E VOLUME 53, NUMBER 2 FEBRUARY 1996

ARTICLES

Chaos in special relativistic dynamics

S. P. Drake, C. P. Dettmann, and N. E. Frankel
School of Physics, University of Melbourne, Parkville Victoria 3052, Australia

N. J. Cornish
Department of Physics, University of Toronto, Toronto, Ontario, Canada M5S 1A7
(Received 26 June 1995)

The study of chaos in relativistic systems (both special and general) is a newly emergent field. The main focus of this paper is the study of the chaotic trajectories of a charged particle in a static electric field. The full special relativistic equations of motion are used. Here we concentrate on motion in a field that is produced by two fixed centers with equal charge. The chaotic nature of these trajectories is investigated by examining the fractal nature of the attractor basin boundary. An examination of how these properties change with respect to fundamental parameters of the problem, such as charges, mass, and charge separation, is undertaken. We emphasize that fractal basin boundaries provide an important characterization of chaos in relativistic dynamics.

PACS number(s): 05.45.+b, 03.30.+p, 47.52.+j, 47.53.+n

I. INTRODUCTION

The classical three-body problem has engaged physicists for over 200 years. In that time, though much progress has been made, solutions have only been found for a few special cases [1]. One such case is the Newtonian motion of an infinitesimal body subject to the $1/r$ potential of two fixed finite bodies. The problem we consider here is the motion of an infinitesimal charged particle about two fixed charged particles described by a special relativistic Hamiltonian. To the best of our knowledge it has not been studied previously. This is a three-body problem with a difference. Trajectories of the test particles are markedly different from the Newtonian model. They behave in a chaotic manner, though in Newtonian mechanics they do not [1]. Comprehensive studies have already been made for the more complicated gravitational analog of this problem. In these studies [2–6] the motion of a charged test particle about two fixed, charged black holes was considered. Herein, the fixed two-center problem is studied in the absence of gravitational interactions and comparisons are made between the two problems. Despite the very different space-time geometry and global causal structure exhibited by the special and general relativistic cases, we find that both systems have very similar chaotic behavior.

A qualitative understanding of the two-center problem can be gained by considering the dynamics in terms of particle motion in an effective potential. In the Newtonian limit the effective potential can be shown to be integrable. Relativistic corrections to the effective potential introduce nonlinearities which cause two qualitative changes in the dynamics. The first change allows trajectories to be captured by the central singularities—even if the trajectories have nonzero angular momentum. The second change in the dynamics comes from the relativistic corrections rendering the effective potential nonintegrable. The study of this second effect will occupy the majority of the paper. The phenomenon of relativistic capture means that we are studying chaos in an open system [7]. Although we will be studying energetically bound trajectories, the dynamics can be considered as a form of chaotic scattering [8] as the captured orbits are not bounded in phase space. Indeed, the capture phenomenon makes the dynamics similar to that seen in Hamiltonian exit systems [9].

The phenomenon of relativistic capture makes the dynamics difficult to study using standard indicators of chaos such as Lyapunov exponents and Poincaré sections as they rely on the existence of long-lived orbits [10]. When attracting regions of phase space exist, we have suggested [2,3] that the best way to study chaos is to examine the nature of the attractor basin boundary (ABB). Indeed, there is a complementary relationship between these methods as Lyapanov exponents are best for studying long-lived trajectories, while ABB's are best for studying trajectories which are quickly captured. An additional reason causes us to favor ABB's over Lyapanov exponents for relativistic systems, namely, Lyapanov exponents are not Lorentz invariant quantities, while the fractal dimension of the ABB's is. Another technique commonly used to study chaos employs Poincaré sections. For open systems these are very difficult to generate as most trajectories quickly escape to various asymptotic regions of phase space. We did manage to generate Poincaré sections for trajectories near stable orbits, but these only account for trajectories forming a set of measure zero in phase space. Rather than struggling to find these rare orbits, we used the quick capture of typical orbits to our advantage and concentrated on generating plots of the basin boundaries. In Sec. IV we argue more strongly for the use of ABB's in determining chaos.

Before launching into this problem, some indication is needed that it may be chaotic. The first signs of this came in [3] where the fractal nature of an ABB was shown for two small mass black holes (small relative to their separation in natural units). The small masses meant that for large regions the space time was approximately Minkowskian. While the chaotic nature of the small mass case suggests that chaos might persist in the special relativistic analog, it is not conclusive. This is because the multi-black-hole space time only truly recovers Minkowski space time when the black-hole masses vanish. No matter how small a nonzero mass black hole might be, it always gives rise to a causal barrier at the horizon, leading to a distinct causal topology not shared by Minkowski space.

To examine the fixed two-center problem in a Minkowski metric, it is sufficient to consider a test particle with charge q and mass m. Choosing the charge to mass ratio so that $q/m \gg 1$ ensures that Coulomb interaction dominates gravity. Our special relativistic version of the fixed two-center problem has led us into electrodynamics. This raises the issue of radiation. It is well known that accelerating charged particles radiate. Under what conditions, if any, can radiation effects be neglected? For example, a classical hydrogen atom would collapse within a microsecond due to radiation losses. In Sec. II we show that it is always possible to select masses and charges so that radiation can be neglected without loss of generality.

Having now established a motivation and suitable model for the special relativistic two-center problem, the outline for the rest of the paper is as follows. Section II establishes the form of the super Hamiltonian used to describe the dynamics. Because we are considering a relativistic extension of a Newtonian problem, it is important to understand why the Newtonian model is integrable while the relativistic model is not. Using the Hamiltonian we are able to find a set of orbits that lie on KAM surfaces, and hence do not exhibit chaos. This is done by obtaining Hamilton's principal function for these orbits. We show that this set of orbits includes small velocity Newtonian-type orbits. For weakly relativistic examples these orbits coexist in phase space with small regions of chaotic orbits.

The relativistic Hamiltonian is not generally separable using the method outlined in Sec. II. It is not even possible to use perturbative techniques since velocities can become ultrarelativistic, as occurs when particles get close to one or another of the charges.

Apart from nonintegrability the relativistic Hamiltonian differs from the Newtonian one in that capture occurs for particles with nonzero angular momentum. Section III examines this phenomenon fully. A set of conditions is found for when capture occurs, leading us to examine the attractor basins. Capture conditions are used as a rough analytic check of the computational integration routine.

The chaotic nature of the system becomes apparent when the attractor basins are studied. The attractor basin boundary (ABB) lies on a fractal set. Section IV is devoted to the generation of ABB's, the calculation of their fractal dimension, and a scale parameter related to their location. An explanation is given as to why we have chosen ABB's as a measure of chaos. Also in Sec. IV is an outline of the computational methods used and a description of how each image was generated.

The last section, Sec. V, is devoted to analyzing the variations of ABB's with fundamental parameters. In this section we discuss how parameters, such as mass and charge, affect the chaotic nature of the system. Results are presented in graphic form. The conclusion made is that while the relativistic two-center problem is chaotic, the measures of chaos appear to vary in an orderly manner.

Finally, in Sec. VI, we develop a conclusion and outline some suggested further work and extensions to the model.

II. FORMALISM

In the Introduction we stated that the effects of radiation would be neglected in this study. In this section we show how this can be done without altering the fundamental nature of the system. The loss of energy due to radiation can be neglected only if the typical rate of change in kinetic energy is very much greater than the power loss due to radiation. The power radiated by a relativistic particle of charge q and mass m is [11]

$$P = \frac{2q^2}{3}\gamma^6 \left[\dot{\mathbf{v}}^2 - (\mathbf{v}\times\dot{\mathbf{v}})^2\right], \tag{2.1}$$

where $\mathbf{v}$ is the particle's velocity, γ the Lorentz boost factor, and the dot represents a derivative with respect to coordinate time. For a charged particle moving in a potential V we have

$$\dot{\mathbf{v}} = \frac{-q}{\gamma m}\left[\nabla V - \mathbf{v}(\mathbf{v}\cdot\nabla V)\right], \tag{2.2}$$

$$\dot{E} = m\dot{\gamma} = -q\mathbf{v}\cdot\nabla V. \tag{2.3}$$

The condition which ensures that radiation reaction can be neglected is

$$P \ll |\dot{E}|\,. \tag{2.4}$$

Using Eqs. (2.1), (2.2), and (2.3) the inequality in (2.4) can be written in terms of the divergence of the potential as

$$P = \frac{2q^4\gamma^2}{3m^2}\left[(\nabla V)^2 - (\mathbf{v}\cdot\nabla V)^2\right] \ll q|\mathbf{v}\cdot\nabla V|. \tag{2.5}$$

If the potential is due to two fixed equal charges, Q, separated by a distance a, i.e., a potential like Eq. (2.13) for $n = 2$, then Eq. (2.5) can be evaluated explicitly. In Sec. III we show that capture occurs for particles that are ultrarelativistic. Since we are looking at the relativistic capture of particles we should examine the ultrarelativistic limit ($|\mathbf{v}| \to 1$) of Eq. (2.5). In this limit we find that the result depends on the type of orbit examined. If the motion is a direct plunge, and $\mathbf{v}$ is parallel to (∇V), then

the γ^2 factor on the left-hand side of Eq. (2.5) is canceled and thus

$$\frac{q^3}{m^2}|\nabla V| \ll 1. \tag{2.6}$$

Taking a typical value for the gradient of the potential to be Q/a^2, we find the above condition can be written as

$$\mathcal{F}^2 \frac{q}{Q} \ll 1, \tag{2.7}$$

with $\mathcal{F}$ defined as

$$\mathcal{F} = \frac{qQ}{ma}. \tag{2.8}$$

We define the scaled electrostatic energy, $\mathcal{F}$, in this way because it proves to be very useful for later calculations. If on the other hand the motion is orbital, close to circular, then $\mathbf{v}$ is perpendicular to (∇V) and the γ^2 persists. However, γ can be estimated from viral theorem considerations to be approximately $\mathcal{F}$ in the ultrarelativistic limit. For orbits such as these Eq. (2.5) now is

$$\mathcal{F}^4 \frac{q}{Q} \ll 1. \tag{2.9}$$

Equations (2.7) and (2.9) imply that radiation can be neglected no matter how large we make $\mathcal{F}$, so long as we make q/Q sufficiently small.

It is worth noting that the factor of γ^2 difference between the direct plunge and circular orbit cases is directly related to the problems found in ring and linear colliders. Radiation loss is never a serious problem in linear colliders.

This means that for orbits which are captured relatively quickly, i.e., with a capture time of order $t_c = a/v$, the effect of radiation can be neglected. Stated another way, with a careful choice of parameters, relativistic capture can dominate the capture due to radiation loss.

Having established a suitable model, we are now ready to examine the dynamical properties of the system. The relativistic equations of motion for a nonradiating particle of charge q in an electromagnetic field can be obtained from the super Hamiltonian [11],

$$\mathcal{H} = \frac{1}{2}(P_\alpha - qA_\alpha)(P^\alpha - qA^\alpha), \tag{2.10}$$

in conjunction with Hamilton's equations,

$$\frac{dx^\alpha}{d\lambda} = \frac{\partial \mathcal{H}}{\partial P_\alpha} \quad \text{and} \quad \frac{dP_\alpha}{d\lambda} = -\frac{\partial \mathcal{H}}{\partial x^\alpha}. \tag{2.11}$$

Here, λ is an affine parameter that is related to the proper time by $\lambda = \tau/m$, where m is the mass of the test particle. The dynamic equations of motion represented here describe a continuous flow of phase space coordinates on a differential manifold. The first of Hamilton's equations relates the canonical momentum, P_α, to the mechanical momentum, p^α:

$$p^\alpha = mu^\alpha = P^\alpha - qA^\alpha, \tag{2.12}$$

where $u^\alpha = dx^\alpha/d\tau$. Since we are considering a static electric field, the spatial components of the vector potential all vanish, $A_i = 0$. The field is generated by placing n fixed charges Q_i at positions (x_i, y_i, z_i) in space, so that $A_0 = V$ is given by

$$V = -\sum_{i=1}^{n} \frac{Q_i}{\sqrt{(x-x_i)^2 + (y-y_i)^2 + (z-z_i)^2}}. \tag{2.13}$$

For fields generated in this way Hamilton's equations can be written as

$$\gamma = \frac{1}{\sqrt{1-\dot{\mathbf{x}}^2}}, \tag{2.14}$$

$$m\gamma = E - qV, \tag{2.15}$$

$$\dot{\mathbf{x}} = \frac{\boldsymbol{\pi}}{\sqrt{\boldsymbol{\pi}^2 + 1}}, \tag{2.16}$$

$$\dot{\boldsymbol{\pi}} = -\frac{q}{m}\nabla V. \tag{2.17}$$

The dot on top of a vector refers to the derivative with respect to coordinate time and $\boldsymbol{\pi} = \mathbf{p}/m$. In most cases these equations cannot be solved analytically. We are thus forced into numerical integration to calculate trajectories. However, if $n = 1$ or 2 some analytic results can be obtained. The case n=1 is the classic special relativistic scattering problem and has been thoroughly studied. A more interesting case occurs for $n = 2$. It is interesting because there is no chaos in the Newtonian version of the problem, nor for certain classes of orbits in the relativistic problem, but for other classes of orbits the system is chaotic. If two equal fixed charges Q are placed at (0,0,-a) and (0,0,a), then Eqs. (2.14)–(2.16) are unchanged by a rescaling of coordinates. By scaling the coordinates so that the fixed charges are at (0,0,-1) and (0,0,1), we can rewrite Eq. (2.17) as

$$\dot{\boldsymbol{\pi}} = -\mathcal{F}\nabla V_0. \tag{2.18}$$

$\mathcal{F}$ is defined as before and V_0 is defined as

$$-V_0 = \frac{1}{\sqrt{x^2 + y^2 + (z-1)^2}} + \frac{1}{\sqrt{x^2 + y^2 + (z+1)^2}}. \tag{2.19}$$

The equations are written in this form so that all parameters that affect the field strength are combined into one scaling quantity, $\mathcal{F}$.

The Newtonian version of this problem has been solved by a number of authors; for example, see [12]. The problem is solved by changing to prolate spheroidal coordinates,

$$x = \sinh\psi \sin\theta \cos\phi, \quad y = \sinh\psi \sin\theta \sin\phi,$$
$$z = \cosh\psi \cos\theta, \tag{2.20}$$

and using the Hamilton-Jacobi separation of variables (see Goldstein [13]). In relativity this method proves to be useful only for a certain class of orbits. In special relativity the super Hamiltonian written in these coordinates is

$$\mathcal{H} = 1/2\left[-\left(S_{,t} - \frac{2qQ\cosh\psi}{a\mathcal{Q}}\right)^2 + \frac{1}{\mathcal{Q}}(S_{,\psi})^2 + \frac{1}{\mathcal{Q}}(S_{,\theta})^2 + \frac{1}{(\sinh\psi\sin\theta)^2}(S_{,\phi})^2\right] = -S_{,\lambda}\,, \tag{2.21}$$

where

$$\mathcal{Q} = \sinh^2\psi + \sin^2\theta \tag{2.22}$$

and S is Hamilton's principal function. Since t, ϕ, and λ are cyclic coordinates, they each have a constant of the motion associated with them. The physical significance of these constants is clear. $E = -S_{,t}$ and $L = S_{,\phi}$ are the total energy and angular momentum of the test particle. The constant associated with λ comes from the fact that the rest mass is conserved. This can be seen explicitly in the following way:

$$-S_{,\lambda} = \mathcal{H} = \frac{1}{2}(-m^2\gamma^2 + \mathbf{p}^2) = -m^2/2\,. \tag{2.23}$$

The generating function S is said to be completely separable if it can be written in the form

$$S(\lambda, t, \psi, \theta, \phi) = S_\lambda(\lambda) + S_t(t) + S_\psi(\psi) + S_\theta(\theta) + S_\phi(\phi). \tag{2.24}$$

The separability of S in the super Hamiltonian is broken by the term

$$\left(\frac{2qQ\cosh\psi}{a\mathcal{Q}}\right)^2. \tag{2.25}$$

This is because any term with $\mathcal{Q}^2$ cannot be separated into a sum of two functions involving θ and ψ only. However, if the term given in Eq. (2.25) is small compared to $4EqQ(\cosh\psi)/(a\mathcal{Q})$, i.e., if

$$\mathcal{F} \ll \left(\frac{\mathcal{Q}}{\cosh\psi}\right)\frac{E}{m} = \frac{\gamma\mathcal{Q}}{\cosh\psi}\,, \tag{2.26}$$

then the system becomes completely separable and

$$S(\lambda, t, \psi, \theta, \phi) = 1/2m^2\lambda - Et + L\phi + S_\theta(\theta) + S_\psi(\psi), \tag{2.27}$$

where

$$S_\psi(\psi) = \int\sqrt{E^2\sinh^2\psi - \frac{L^2}{\sinh^2\psi} + \frac{4EqQ^2\cosh\psi}{a} - m^2\sinh^2\psi + \alpha}\,d\psi \tag{2.28}$$

and

$$S_\theta(\theta) = \int\sqrt{E^2\sin^2\theta - \frac{L^2}{\sin^2\theta} + -m^2\sin^2\theta + \alpha}\,d\theta. \tag{2.29}$$

The fourth constant of motion, α, is

$$\alpha = E^2\sinh^2\psi - \frac{4EqQ\cosh\psi}{a} - (S_{,\psi})^2 - \frac{L^2}{\sinh^2\psi} - m^2\sinh^2\psi, \tag{2.30}$$

$$= E^2\sin^2\theta - (S_{,\theta})^2 - \frac{L^2}{\sin^2\theta} - m^2\sinh^2\theta. \tag{2.31}$$

Equations (2.28) and (2.29) can be used in conjunction with [13],

$$\beta_i = \frac{\partial S_{q_i}(q_i)}{\partial\alpha_i}, \tag{2.32}$$

to find explicit solutions involving time. The β_i's are the initial conditions, the q_i's refer to phase-space coordinates as well as time, and the α_i's are constants of the motion associated with each coordinate. Such orbits are said to be integrable and hence not chaotic. The KAM [14–16] theorem states that if a small nonlinear perturbation is added to the Hamiltonian, regions of regular motion will continue to occur. This implies that if relativistic effects are small, then there will exist some regions in phase space which do not have chaotic trajectories.

The inequality in Eq. (2.26) gives a condition for the type of orbits that are integrable. As expected, these include Newtonian-type orbits where $\mathcal{Q}$ is large, i.e., the field is weak and $E \approx m$. If $\mathcal{Q}$ is large, then ψ is large. For large ψ, $\mathcal{Q} \approx \sinh^2\psi$ and $\cosh\psi \approx \sinh\psi$. The inequality in Eq. (2.26) now becomes

$$\gamma_0 \gg \frac{\mathcal{F}}{\sinh\psi}, \tag{2.33}$$

where γ_0 is the value of γ at time $t = 0$. Equation (2.33) is satisfied for certain relativistic orbits as well as Newtonian ones. An example of an orbit which does not escape yet does not collapse is shown in Fig. 1. Figure 1 was generated using a fourth-order adaptive step size Runge-Kutta routine [17]. In this figure $\mathcal{F} = 0.06$ and the motion appears to be periodic. This orbit is not typical of the type studied here. Collapse to a singularity does not occur, hence radiation effects cannot be neglected as they are cumulative. For this reason, we chose to study orbits in which the inequality in Eq. (2.26) is seldom obeyed. In the next section we examine what happens when Eq. (2.26) is not satisfied. In the relativistic limit the equations of motion are not completely separable in prolate spheroidal coordinates. This does not prove that the system is nonintegrable, but it does show that if the

system is chaotic, the chaos is due solely to relativistic effects.

III. RELATIVISTIC CAPTURE

In Newtonian mechanics, trajectories with nonzero angular momentum do not collapse into a singularity. In relativity, even trajectories with nonzero angular momentum can terminate at the central singularity [18]. This effect can be easily demonstrated in the case of one fixed center. The spherical symmetry in this case allows the motion to be modeled by a one-dimensional effective potential. The super Hamiltonian may be used to obtain the condition

$$m^2\left(\frac{dr}{d\tau}\right)^2 + V_{eff}^2 = E^2 \,. \tag{3.1}$$

Here τ is the proper time along the trajectory and the effective potential is given by

$$V_{eff}^2 = m^2 - \frac{2EqQ}{r} + \frac{L^2 - q^2Q^2}{r^2} \,. \tag{3.2}$$

In the Newtonian limit this reduces to

$$V_{N\,eff}^2 = m^2 - \frac{2mqQ}{r} + \frac{L^2}{r^2} \,. \tag{3.3}$$

Near $r = 0$ the Newtonian effective potential is always dominated by the repulsive angular momentum barrier L^2/r^2. For relativistic orbits the repulsive barrier only exists when $L > qQ$. Trajectories with $L < qQ$ can be captured.

It is worth noting that in the ultrarelativistic limit the angle θ between the position and the momentum vectors is given near $r = 0$ by

$$\theta \approx \arcsin\frac{L}{qQ}. \tag{3.4}$$

This means that θ is constant, hence the trajectory is a spiral of finite length and therefore takes a finite time to be captured.

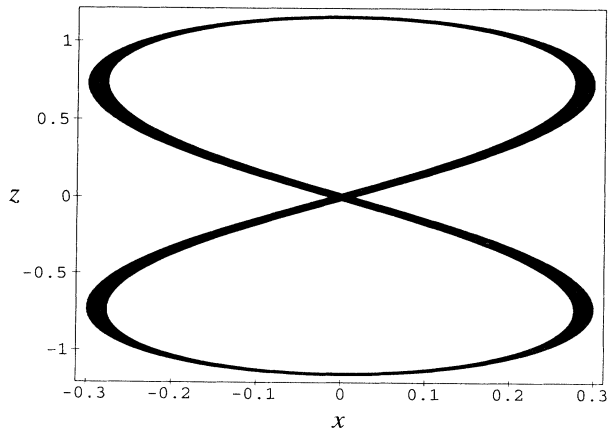

FIG. 1. A trajectory with $\mathcal{F} = 0.03$ and initial conditions ($x = 4.5, y = 2.0$, and $\boldsymbol{\pi} = 0$).

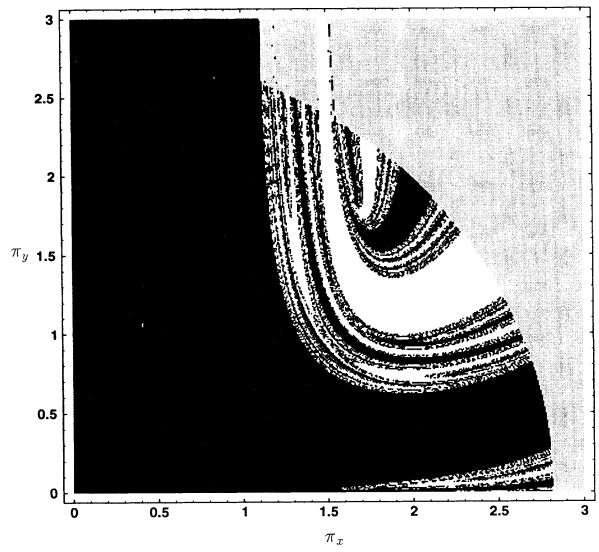

FIG. 2. A section of the attractor basins for $x = 0$ and $\mathcal{F} = 1$.

Figure 2 was generated by following the trajectories of particles that start at the origin with various initial values of π_x and π_z. Trajectories that finish at (0,0,-a) are labeled black, those that finish at (0,0,a) are labeled white, and those that do not collapse to a singularity, within a finite time, are labeled grey. The trajectories labeled grey are stable in the sense that doubling the maximum time along a given trajectory did not alter the size or shape of the grey regions. Figure 2 is an 840×840 plot with $\mathcal{F} = 1$. The two most noticeable features of this figure, apart from its regions of complexity, are the escape of particles with a $\|\boldsymbol{\pi}\| \gtrsim 2.8$ and the capture of particles with a $\pi_x \lesssim 1$. Both these results can be shown analytically.

If a particle is set in motion at the origin, then in order for its motion to be bounded it must have an energy less than or equal to the rest mass of the particle. This implies that

$$\|\vec{\pi}\| \leq \sqrt{(2\mathcal{F}+1)^2 - 1}. \tag{3.5}$$

For $\mathcal{F} = 1$, Eq. (3.5) tells us that escape occurs for $\|\vec{\pi}\| \geq \sqrt{8} \approx 2.8$. The capture of particles with $\pi_x \lesssim 1$ can be shown by considering the simpler case where the potential due to the second fixed charge is ignored. We can justify this by assuming that momentum in the z direction is unaffected until the particle is so close to one charge that the other can be ignored. Using the condition $L < qQ$, in conjunction with the fact that $L = am\pi_x$ at the origin, the capture condition becomes

$$\pi_x \lesssim \mathcal{F}. \tag{3.6}$$

At this point we note that capture occurs for similar conditions in general relativity. For a single, extremely charged black hole the effective potential reads

$$V_{eff}^2 = \frac{1}{(1+M/r)^4}\left[m^2\left(1+\frac{M}{r}\right)^2 + \frac{L^2}{r^2}\right], \quad (3.7)$$

in isotropic coordinates [19,20]. In these coordinates $r = 0$ corresponds to a surface of finite area (the horizon) and not the central singularity. The singularity lies below $r = 0$. As we stated in the Introduction, the global causal topology is different for the special and general relativistic situations due to the horizon at $r = 0$, but it is worth noting that they share the same causal structure for $r > 0$. The potential (3.7) has a maximum at

$$r = \frac{L^2 - 2M^2m^2 - L\sqrt{L^2 - 4M^2m^2}}{2Mm^2}. \quad (3.8)$$

Particles with an energy which exceeds the maximum value of the potential barrier are subject to capture by the black hole. For ultrarelativistic particles the capture condition reads

$$L < 2\sqrt{4(E/m)^2 - 1}(Mm), \quad (3.9)$$

while for nonrelativistic particles the condition becomes

$$L < \sqrt{2}(2+\sqrt{13})^{1/2}(Mm). \quad (3.10)$$

We see that termination of trajectories at the central singularity is a standard feature of relativistic dynamics, both special and general.

IV. FRACTAL ATTRACTOR BASIN BOUNDARIES

The capture of particles leads us to examine the nature of the attractor basin boundary. Studies of chaotic systems often focus on the determination of Lyapunov exponents as a measure of chaos [21]. The Lyapunov exponents λ_k in flat space time are defined by choosing a point x in phase space, at the center of a ball of radius $\epsilon \ll 1$. After a time t the ball evolves into an ellipsoid with semiaxes $\epsilon_k(t)$, where k ranges from one to the dimension of the phase space. The Lyapunov exponents are

$$\lambda_k(x) = \lim_{t\to\infty}\lim_{\epsilon\to 0}\frac{1}{t}\ln\frac{\epsilon_k(t)}{\epsilon}, \quad (4.1)$$

assuming the limits exist. The λ_k are constant along a trajectory, and are often constant over larger regions of phase space such as the basin of an attractor. However, there are problems with this approach. First, the existence of a positive Lyapunov exponent is not enough to determine if a system is chaotic [22]. Integrable systems can have *isolated* unstable periodic orbits. For example, the Newtonian version of the fixed two-center problem (which is not chaotic) has a set of positive Lyapunov exponents for orbits that are perpendicular to the z axis. Second, the computation of Lyapunov exponents requires setting a finite time limit, thus inducing an error. If particles are captured too quickly this error is large.

In the general relativistic problem the topology of the ABB was used as a measure of chaos. A particularly appealing feature of this method in general relativity is that ABB's furnish a coordinate independent measure of chaos. While this is not an issue in special relativity, the ABB's continue to recommend themselves as a measure of chaos since they do not require long-lived orbits.

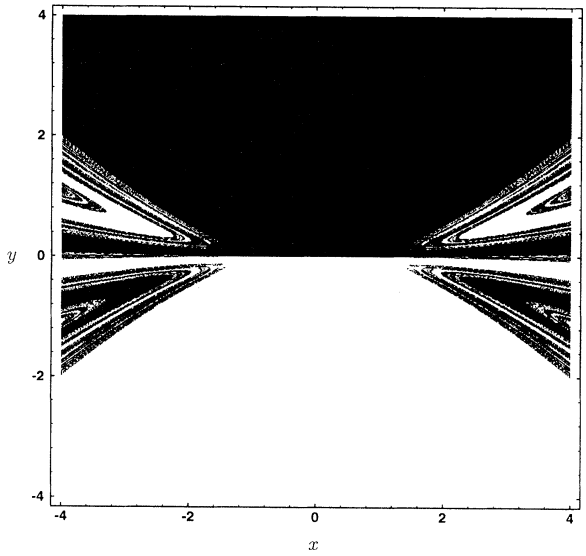

FIG. 3. A section of attractor basins for $\pi = 0$ and $\mathcal{F} = 1$.

In chaotic systems the ABB will lie on a fractal set, while in nonchaotic systems they will not. Using this approach we do not have the problems associated with finite time capture. In fact, the faster the capture the better since it reduces computational time. To determine if the ABB lies on a fractal set we must measure the fractal dimension of the ABB. One of the distinguishing features of fractal sets is their noninteger fractal dimensions. This gives us an unambiguous way of determining the chaotic nature of the system.

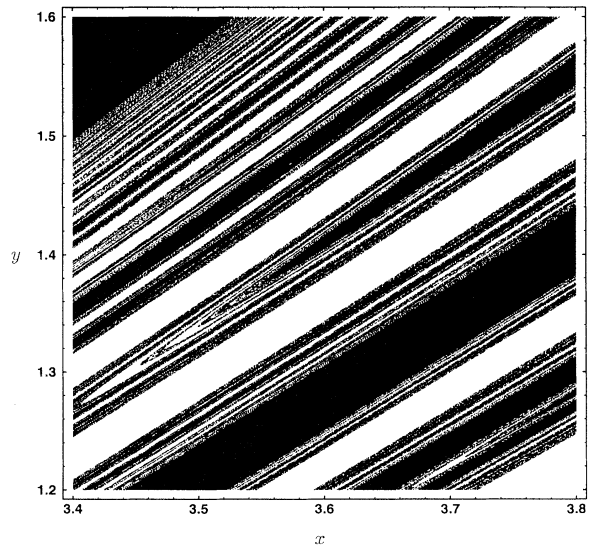

FIG. 4. Magnification of Fig. 3.

If the y axis is chosen so that it is perpendicular to the plane of motion, then the ABB's lie in a four-dimensional phase space. Clearly, it is not possible to generate graphics for these. A two-dimensional slice of this phase space must be taken in order to generate tangible pictures. All the ABB's generated for this paper are on an 840×840 grid, and are generated in the same manner as Fig. 2. Most of the phase-space slices are done by setting the initial momentum to zero. This not only reduces computational time, by enabling most trajectories to be captured, but makes comparison with the general relativistic study easier.

The ABB for $\mathcal{F} = 1$ is shown in Fig. 3. We first notice that it appears to have all the expected symmetries. One of the most fascinating features of this image is the large portion of the ABB that appears to have a fractal nature. Repeated magnification of this image, Figs. 4, 5, and 6, reveals detailed structure on finer and finer scales. This is one of the properties that all fractals have in common. Punctuated between these regions of fractal phase space are regions which are distinctly nonfractal.

Having decided what slice of the ABB phase space to measure, the next step is to find the fractal dimension. There are a number of definitions of fractal dimensions in the literature. The one that is used here is called the box dimension [23]. We will use it because of its ease in computation and because of its common use.

Consider the bounded set F, which is a subset of $\mathbb{R}^n$, then $N_\epsilon(F)$ is the least number of sets of cubes of length ϵ which completely covers the set F. By definition the box dimension for F is

$$\dim_{BF} = -\lim_{\epsilon \to 0} \frac{\ln N_\epsilon(F)}{\ln \epsilon}. \tag{4.2}$$

Because our set is not defined by any known iterative map it is not possible to find the dimension analytically. This means we are forced to use computational techniques. From Eq. (4.2) we can see that the negative gradient of $\ln N_\epsilon$ versus $\ln \epsilon$ gives us the box dimension.

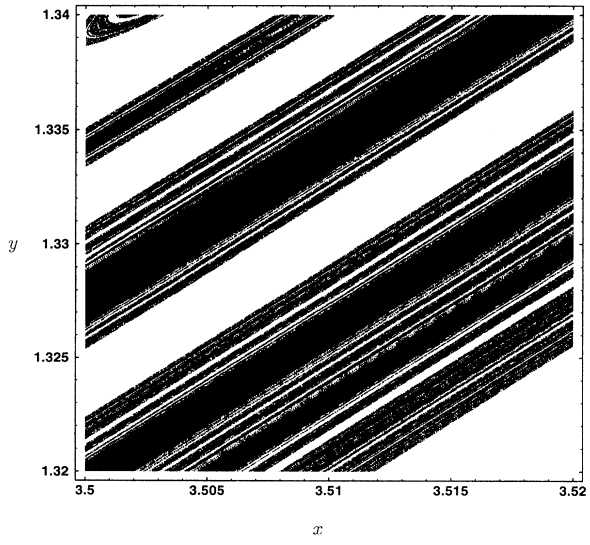

FIG. 5. Magnification of Fig. 4.

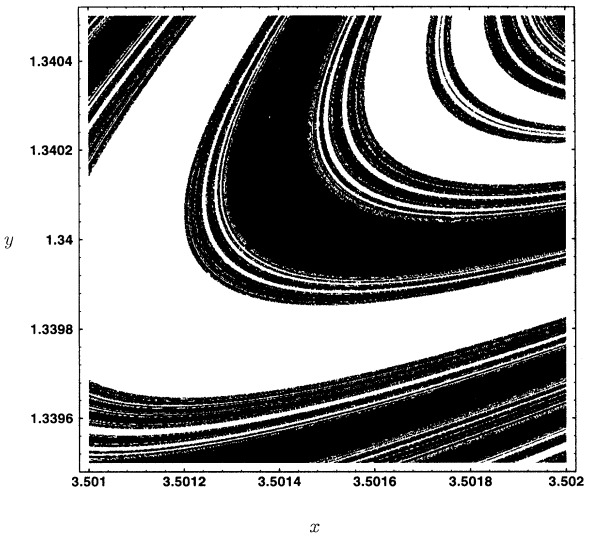

FIG. 6. Magnification of Fig. 5.

The set we wish to examine is the set of points which lie on the ABB in some region of phase space. To do this the whole region of interest is covered by a grid. Cubes of length ϵ are constructed from this grid. If a cube contains two or more grid points that fall into different attractors, then that cube lies on the ABB. Put more formally, each point x_i has an attractor associated with it, A_{x_i}. A cube $B(x_0, \epsilon)$ of length ϵ and centered at x_0 is said to lie on the ABB if

$$\forall \epsilon > 0 \; \exists \; x_1, x_2 \; : \; \{x_1, x_2 \in B(x_0, \epsilon)\}$$

and (4.3)

$$\{x_1 \neq x_2, A_{x_1} \neq A_{x_2}\}.$$

To find the limit in Eq. (4.2) the number of cubes N_ϵ of length ϵ that lie on the ABB is counted. This is repeated for as many values of ϵ as possible. Plotting $\ln N_\epsilon$ against $\ln \epsilon$ gives a straight line. The gradient of this line, which is the negative of the box dimension, is calculated using a χ^2 fit.

In order to maximize the accuracy in calculating the box dimension, the greatest number of values for ϵ is needed, the implication being that the size of the grid should be chosen so that as many combinations of cubes as possible completely cover the phase-space slice. Therefore, the attractor basin is divided into an 840×840 grid since 840 has 31 factors. This is the largest number of factors for any number below 1000, the number chosen as an upper limit due to program running time.

The box dimension for Fig. 7 was calculated in the manner described above. The result is shown in Fig. 8. This figure shows that most of the points do in fact lie on a straight line. This gives us confidence that these images are in fact true fractals and not just roundoff errors in the computer.

On closer inspection, it can be seen that for large ϵ

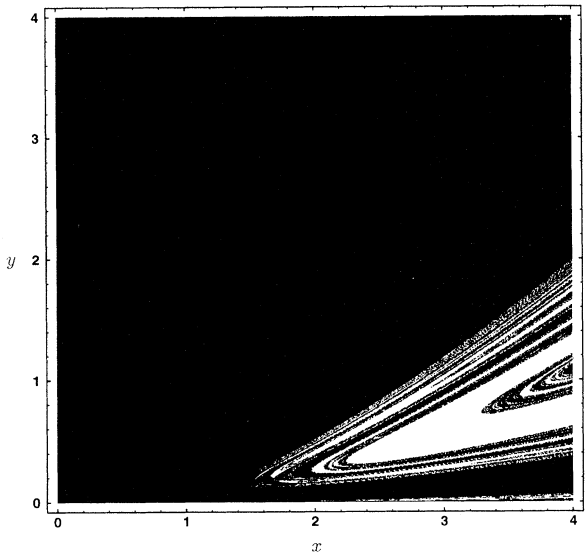

FIG. 7. A subsection of attractor basins in Fig. 3.

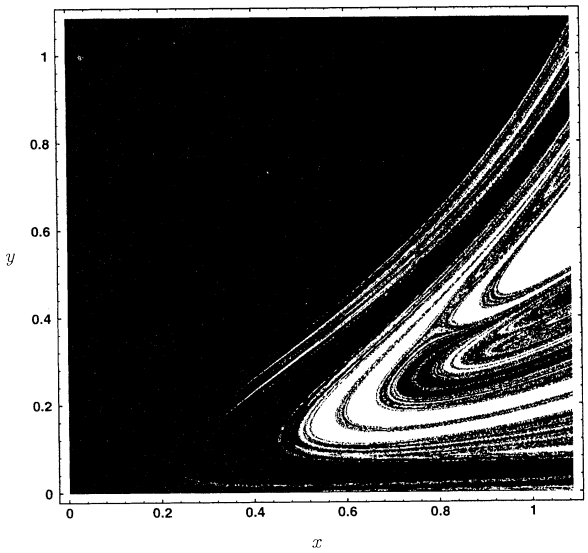

FIG. 9. A section of attractor basins for $\pi = 0$ and $\mathcal{F} = 0.03$.

there seem to be to many cubes (a cube is a square in two dimensions) that lie on ABB. The reason for this is quite clear. If we make ϵ too large, i.e., by dividing the phase space into four sections, then all the cubes will most likely contain both black and white. This means essentially that all cubes lie on the boundary, i.e., we have overcounted.

A second and slightly more subtle complication occurs for small ϵ. From Eq. (4.2) it would seem that the smaller the value of ϵ, the better. The problem comes about because the color of a subcube is defined by only one point in that subcube. Imagine, for example, that that subcube lies on the boundary and is half-filled with black and half with white. This would mean there was a 50%-50% chance that this cube would be labeled black or white. If our cube ϵ was made up of four such subcubes, then there would be a 1/8 chance that this cube would not be counted as being on the boundary. If ϵ was made up of nine such subcubes, then there is a $(1/2)^8$ chance that it will not be counted. For this reason we get fewer counts than we expected for small ϵ.

To eliminate both these errors the first three and last six points of Fig. 8 are removed before determining the gradient. The result is that the fractal dimension of the ABB for Fig. 3 and hence Fig. 7 is $d_B = 1.75 \pm 0.01$.

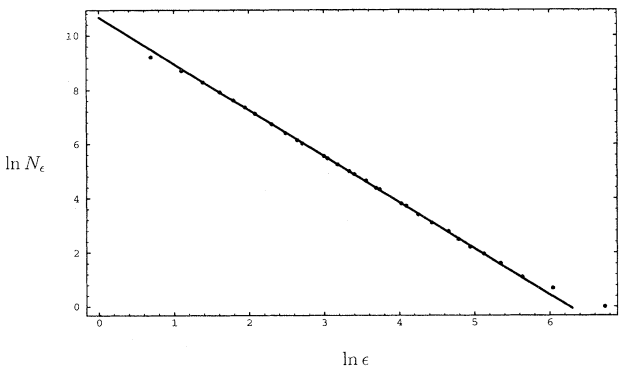

FIG. 8. Calculation of the box dimension for $\mathcal{F} = 1$.

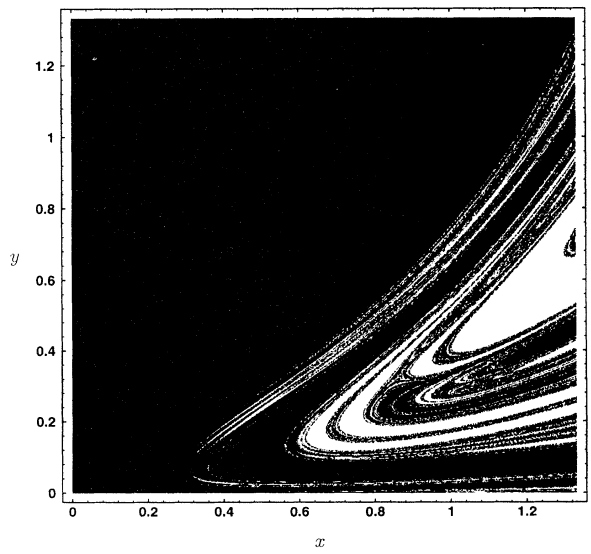

FIG. 10. A section of attractor basins for $\pi = 0$ and $\mathcal{F} = 0.05$.

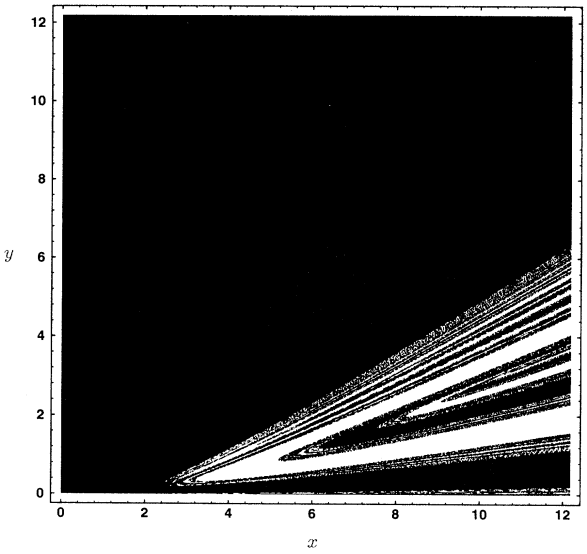

FIG. 11. A section of attractor basins for $\pi = 0$ and $\mathcal{F} = 3$.

V. DEPENDENCE OF FRACTAL STRUCTURE ON $\mathcal{F}$

Since we are using the ABB as a measure of chaos in the system, we need to ask ourselves how does it depend on the field strength? It is of fundamental importance not only to determine whether or not a system is chaotic, but also how the chaotic nature changes with the fundamental parameters. In Figs. 9–12 we see a major change of fractal structure in different regions and for different values of $\mathcal{F}$. The graphics make the differences explicitly apparent. To study this strong dependence on $\mathcal{F}$, we adjust the scaling parameter $\mathcal{F}$ and remeasure the box dimension. However, the dimension for a given scaling parameter $\mathcal{F}$ varies depending on the portion of the attractor basin examined. For this reason we chose to measure the box dimension within the same relative region each time. How the region is chosen is related to the scale point, described below.

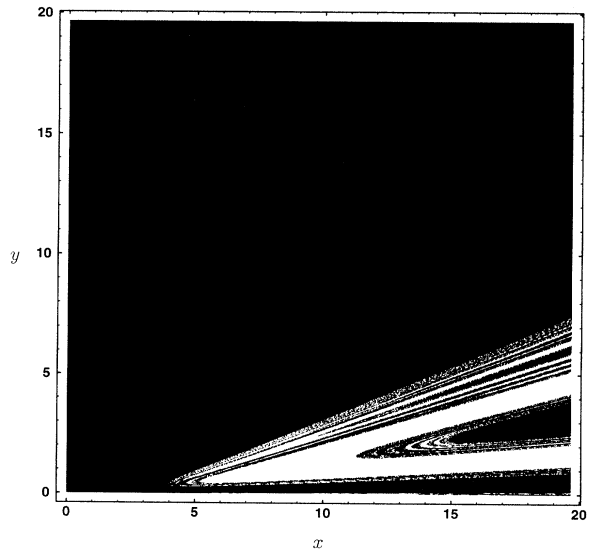

FIG. 12. A section of attractor basins for $\pi = 0$ and $\mathcal{F} = 50$.

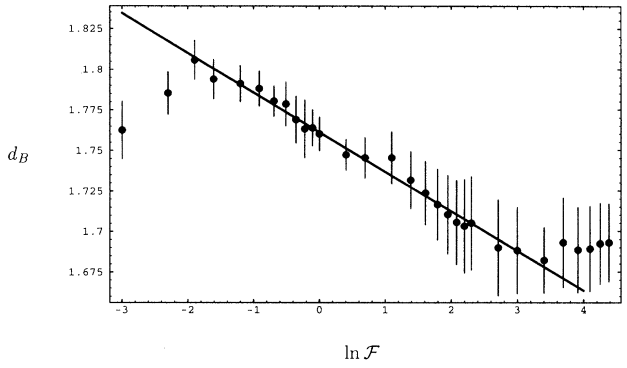

FIG. 13. The effect varying $\mathcal{F}$ has on the box dimension.

Apart from the box dimension, there is also another measure of the onset of chaos in the system. For the purposes of this paper it is called the scale point P. The scale point is the smallest value of x at which a particle with zero initial momentum does not fall into the nearest charge. This point represents the least lower bound of the fractal set. As such, it indicates that a set of unstable trajectories with nonzero measure exists beyond this point.

The scaling point leads naturally to deciding what region of phase space the box dimension is measured for. Somewhat arbitrarily, the box dimension for each $\mathcal{F}$ is measured in a square of phase space whose length is five times P. Each square is located so that the bottom left-hand corner is at the origin.

Figures 13 and 14 show how the dimension and scale point vary with $\ln \mathcal{F}$. The error bars in Fig. 13 are the

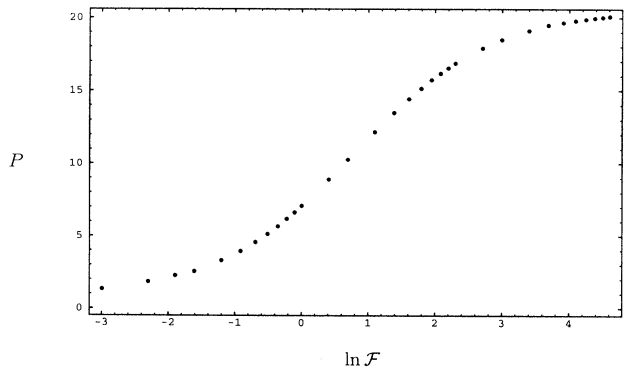

FIG. 14. The effect varying $\mathcal{F}$ has on the scaling point.

standard deviation of points from the line of best fit used to determine the gradient. In both cases it is clear that there exists a functional relationship between $\mathcal{F}$ and what is being measured. Determining this functional relationship is not trivial. Both plots show that for $\mathcal{F} \lesssim 20$ the fractal nature of the ABB changes quite significantly. In this region both the box dimension and scale point are both very sensitive to $\mathcal{F}$. For values of $\mathcal{F} \gtrsim 20$ the scaling point and box dimension seem to approach a limit.

Figure 13 can reasonably be fitted to a straight line for values of $\mathcal{F}$ between about 0.15 and 30. In this region the functional relationship between box dimension d_B and $\mathcal{F}$ is

$$d_B \approx 1.76 - 0.02 \ln \mathcal{F}. \tag{5.1}$$

Figure 14, on the other hand, cannot reasonably be fitted to a straight line for any significant range of $\mathcal{F}$ values. Its characteristics resemble more of an arctan-type function.

These results now complete the study of the relativistic fixed two-center problem. This work and the work on the general relativistic problem has shown that the fixed two-center problem is chaotic. In fact, the Newtonian limit is unique in that it is integrable. The chaotic nature of this system is nicely shown by the fractal nature of the ABB.

VI. CONCLUSION AND FURTHER WORK

We have established that the simplest three-body problem, motion with two fixed centers, is not integrable when special relativistic effects are taken into account. While this result has already been discovered in the context of general relativity [4], we now see that it is not due to any exotic behavior caused by black holes. In particular, it should not be attributed to the nonlinearity of the gravitational force. Chaos is present even when the potentials generated by the two centers obey the superposition principle. Clearly, it is the relativistic description of the kinematics, and not the loss of the superposition principle, which renders the special and general relativistic two-center problem chaotic. To be specific, it is the nonlinear way in which the potential energy enters the relativistic Hamiltonian that renders the dynamics nonintegrable.

Our study can be summarized as follows. After establishing that radiation reaction could be neglected, we employed the Hamilton-Jacobi method to discover under what conditions the system was integrable. The integrable cases were found to include Newtonian-type orbits. For non-Newtonian orbits some properties unique to the relativistic Hamiltonian were found. One of these properties was the capture of particles with nonzero angular momentum. This meant that relativistic particles could spiral into one of the charges within a finite time. As a consequence of this we were able to study the attractor basin boundaries. These ABB's turned out to be fractals and hence indicated that the system was chaotic. To study how the fractals changed with $\mathcal{F}$, both the scaling point and box dimension were examined.

Though this study is comprehensive, there is still further work that could be done. For example, radiation effects could be added. This would mean that orbits which are not ultrarelativistic will be captured due to loss of energy. Some other dissipative force such as a viscous drag could also be included. Lyapunov exponents could be calculated for orbits that do not terminate in a finite time. A possible connection between the dimension of the ABB and the magnitude of the Lyapunov exponents could also be investigated.

ACKNOWLEDGMENTS

S.D. and C.D. would like to thank the Australian Postgraduate Program for support during the completion of this work. S.D. would also like to thank Peter Drake for the correction of many spelling and grammatical errors. N.J.C. would like to thank the University of Melbourne School of Physics for their hospitality during his visit.

[1] M. C. Gutzwiller, *Chaos in Classical and Quantum Mechanics* (Springer-Verlag, New York, 1990).
[2] C. P. Dettmann, N. E. Frankel, and N. J. Cornish, Phys. Rev. D **50**, R618 (1994).
[3] C. P. Dettmann, N. E. Frankel, and N. J. Cornish, Fractals **3**, 161 (1995).
[4] G. Contopoulos, Proc. R. Soc. London, Ser. A **431**, 183 (1990).
[5] G. Contopoulos, Proc. R. Soc. London, Ser. A **435**, 551 (1991).
[6] G. Contopoulos and H. Papadaki, Celest. Mech. Dyn. Astron. **55**, 47 (1993).
[7] P. Gaspard and F. Baras, in *Microscopic Simulations of Complex Hydrodynamical Phenomena* (Plenum Press, New York, 1992).
[8] B. Eckhart and C. Jung, J. Phys. A **19**, L829 (1986); C. Jung and H. Scholz, *ibid.* **20**, 3607 (1987); M. Hénon, Physica D **33**, 132 (1988); G. Contopoulos, *ibid.* **64**, 310 (1993).
[9] S. Bleher, C. Grebogi, E. Ott, and R. Brown, Phys. Rev. A **38**, 930 (1988).
[10] G. Benettin, L. Galgani, and J. M. Strelcyn, Phys. Rev. A **14**, 2338 (1976).
[11] J. D. Jackson, *Classical Electrodynamics* (Wiley, New York, 1975).
[12] C. L. Charlier, *Die Mechanik des Himmels* (von Veit, Leipzig, 1902).
[13] H. Goldstein, *Classical Mechanics* (Addison-Wesley, Reading, 1980).
[14] A. N. Kolomogorov, Proc. Int. Conf. Math. **1**, 315 (1957).

[15] V. I. Arnold, Russ. Math. Surv. **18**(5), 9 (1973).
[16] J. K. Moser, Nachr. Akad. Wiss., Gottingen, Math. Phys. Kl **2**, 1 (1962).
[17] W. H. Press *et al.*, *Numerical Recipes in C* (Cambridge University Press, Cambridge, 1992).
[18] L. D. Landau and E. M. Lifshitz, *The Classical Theory of Fields* (Pergamon, New York, 1971), p. 93.
[19] S. D. Majumdar, Phys. Rev. **72**, 390 (1947).
[20] A. Papapetrou, Proc. R. Irish Acad. **A51**, 191 (1947).
[21] I. Shimada and T. Nagashima, Prog. Theor. Phys. **61**, 1605 (1979).
[22] C. J. Thompson, *Lecture Notes on Dynamical Systems and Chaos* (University of Melbourne, Melbourne, 1992).
[23] K. Falconer, *Fractal Geometry; Mathematical Foundations and Applications* (Wiley, Chichester, 1990).

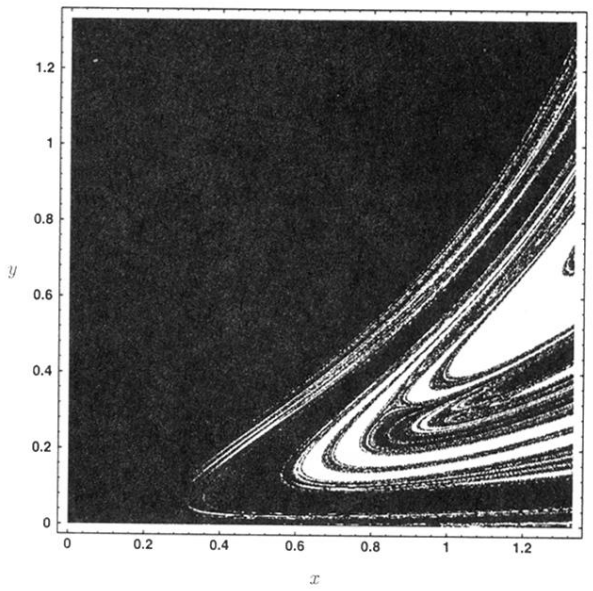

FIG. 10. A section of attractor basins for $\pi = 0$ and $\mathcal{F} = 0.05$.

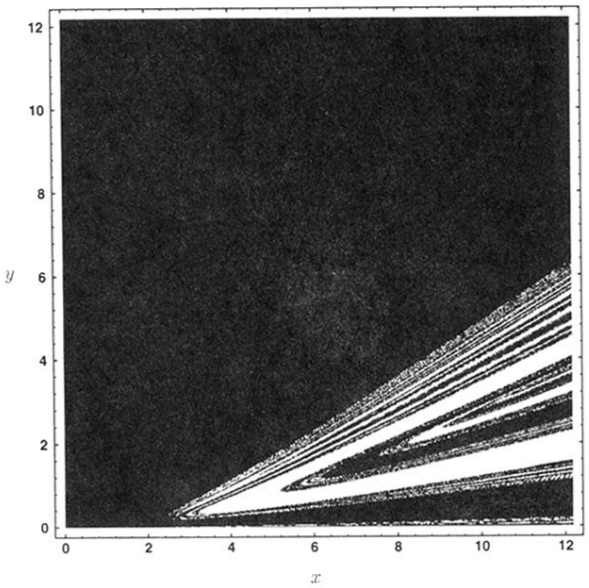

FIG. 11. A section of attractor basins for $\boldsymbol{\pi} = 0$ and $\mathcal{F} = 3$.

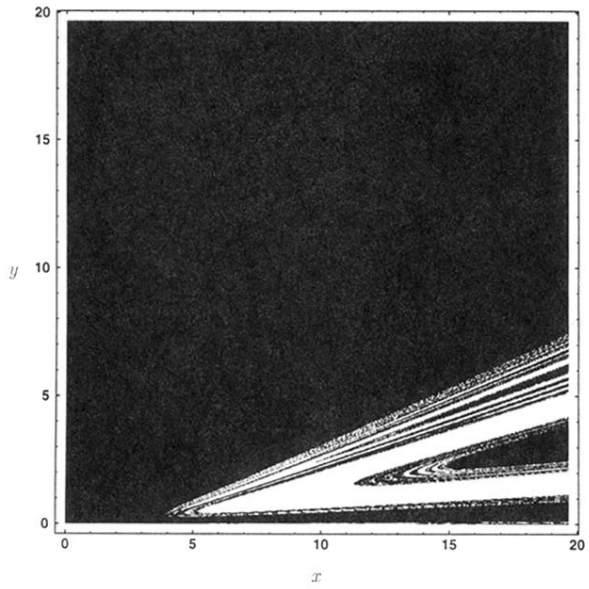

FIG. 12. A section of attractor basins for $\pi = 0$ and $\mathcal{F} = 50$.

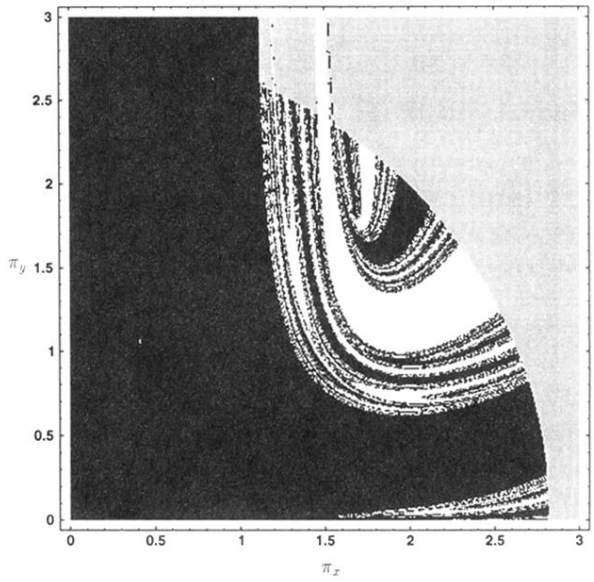

FIG. 2. A section of the attractor basins for $x = 0$ and $\mathcal{F} = 1$.

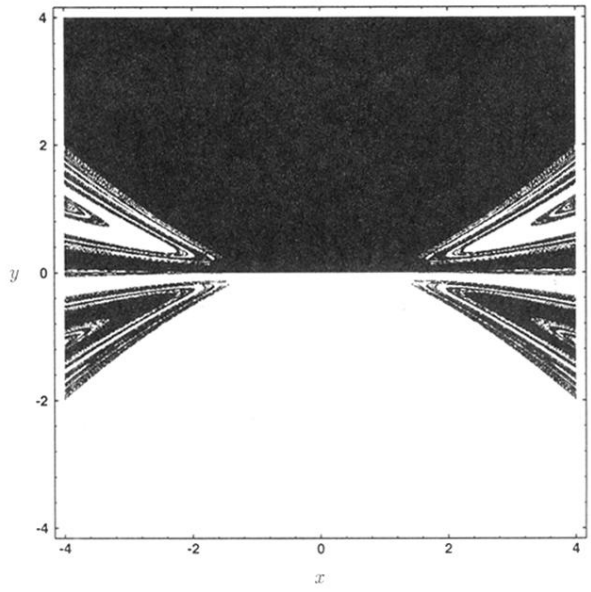

FIG. 3. A section of attractor basins for $\boldsymbol{\pi} = 0$ and $\mathcal{F} = 1$.

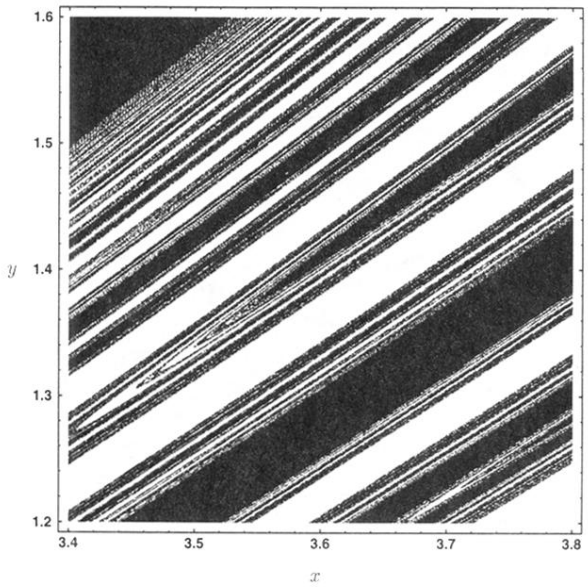

FIG. 4. Magnification of Fig. 3.

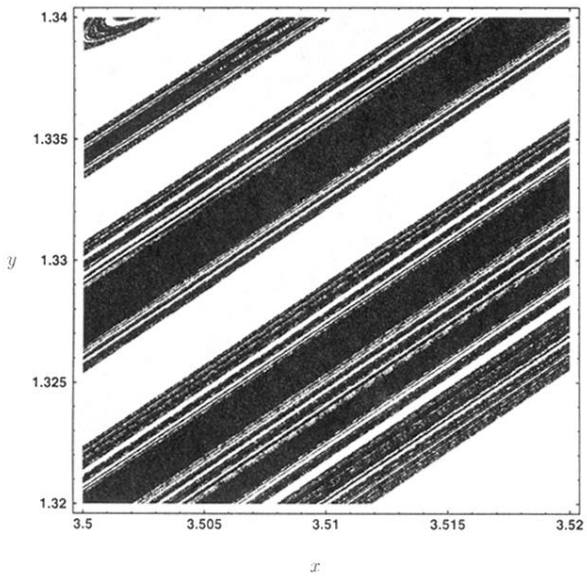

FIG. 5. Magnification of Fig. 4.

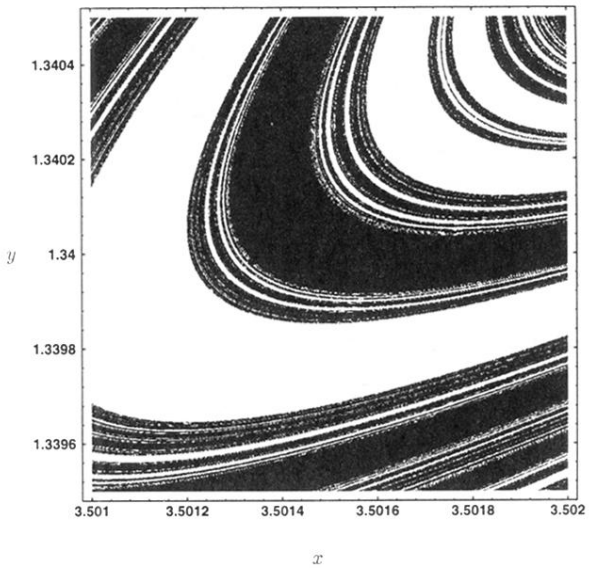

FIG. 6. Magnification of Fig. 5.

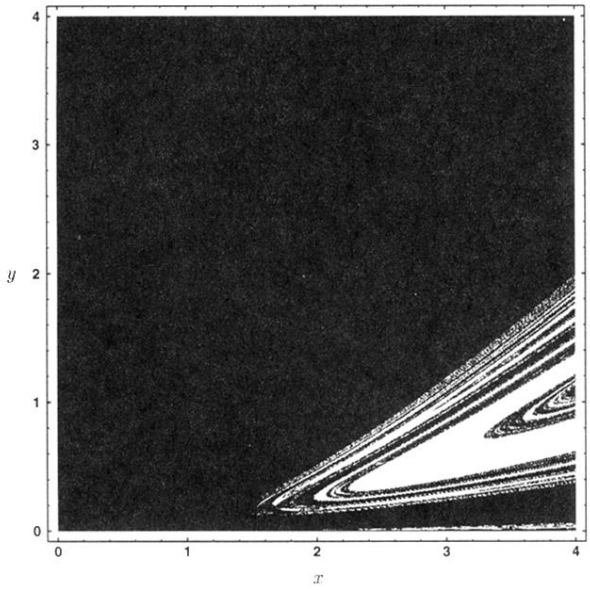

FIG. 7. A subsection of attractor basins in Fig. 3.

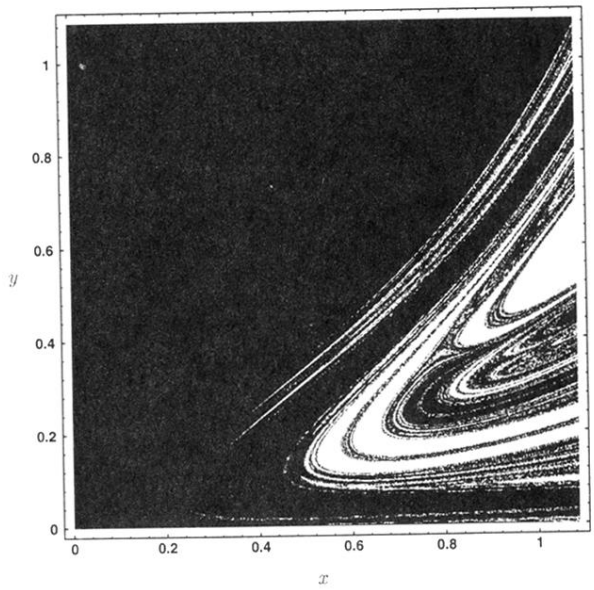

FIG. 9. A section of attractor basins for $\pi = 0$ and $\mathcal{F} = 0.03$.